

# Delayed responses of the oceanic Beaufort Gyre to winds and sea ice motions: influences on variations of sea ice cover in the Pacific sector of the Arctic Ocean

Eri Yoshizawa · Koji Shimada · Ho Kyung Ha ·  
Tae Wan Kim · Sung Ho Kang · Kyung Ho Chung

Received: 6 August 2014 / Revised: 5 February 2015 / Accepted: 12 February 2015 / Published online: 3 March 2015  
© The Oceanographic Society of Japan and Springer Japan 2015

**Abstract** In the late 2000s, the dominant sea ice type in the Arctic Ocean changed from multi-year ice to first-year ice. In this condition, winter growth of first-year ice and resultant ice thickness at the melt onset are key pre-conditions on whether sea ice can survive or will disappear during the following summer. The growth rate strongly depends on upper ocean thermal conditions. In the Pacific sector of the Arctic Ocean, the warm Pacific Summer Water, which is a major heat source affecting the sea ice growth, is transported toward the basin by the oceanic Beaufort Gyre, driven by winds and sea ice motions, but the response time scale of the oceanic Beaufort Gyre to surface forcing has been unclear until now. In the present study, we examine the relationship between the ocean dynamic height near the Northwind Ridge as a proxy of the northward volume transport and curls of winds and sea ice velocities, using multiple regression models that evaluate relative contributions of past surface forcing to the current state of the oceanic Beaufort Gyre. As a result, the time scale of the delayed oceanic response in 2006–2012 was estimated to be about 3 years. Taking into account the response time scale, the multiple regression model using the satellite-derived sea ice motion data successfully reconstructed the observed variations of ocean dynamic heights

within an accuracy of 0.2 dynamic cm, which corresponded to about 2 % of the amplitude of the observed variations.

**Keywords** Arctic Ocean · Oceanic Beaufort Gyre · Sea ice motion · Sea ice reduction · Pacific Summer Water

## 1 Introduction

In recent years, the anomalous sea ice retreat into the central Arctic basin has been mainly observed in the Pacific sector of the Arctic Ocean (Kwok and Rothrock 2009; Markus et al. 2009). First-year ice has replaced multi-year ice as the dominant sea ice type in the Arctic Ocean (Maslanik et al. 2011; Comiso 2011; Polyakov et al. 2012). In this situation, the thickness of first-year ice at the melt onset, which is influenced by sea ice growth in winter, is an important precondition of whether or not sea ice can survive during the following summer. The sea ice growth in winter is influenced by thermohaline stratifications in the upper ocean. In the Pacific sector of the Arctic Ocean, one of the major heat inputs to the upper ocean just beneath the surface mixed layer is primarily controlled by advection of the warm Pacific Summer Water (PSW). PSW is transported into the Canada Basin (Fig. 1a) by the oceanic Beaufort Gyre (OBG), driven by winds and sea ice motions. Therefore, the volume transport of the OBG is a key parameter to determine upper oceanic heat contents in the basin.

Based on the geostrophic balance, there is a direct way to calculate the upper ocean circulation from spatial distributions of the sea surface height measured by satellite-installed altimeters. The amplitude of the temporal variations of the ocean dynamic height (ODH) from hydrographic data in the Canada Basin was about 10 dynamic

E. Yoshizawa (✉) · K. Shimada  
Graduate School of Tokyo University of Marine Science  
and Technology, Konan 4-5-7, Minato-ku 108-8477, Japan  
e-mail: d122018@kaiyodai.ac.jp

H. K. Ha  
Department of Ocean Sciences, Inha University,  
Incheon 402-751, Korea

T. W. Kim · S. H. Kang · K. H. Chung  
Korea Polar Research Institute, Incheon 406-840, Korea

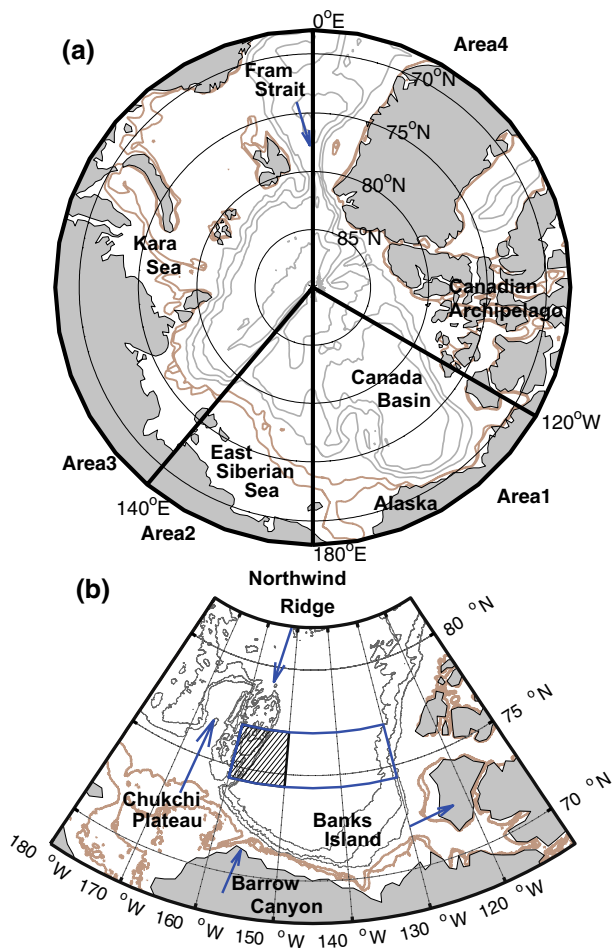


**Fig. 1** Bottom topography of study area. Grey (brown) contours indicate seafloor topographies deeper (shallower) than 1000 m (100 m), contour interval 1000 m (50 m). **a** The Arctic Ocean. Areas 1–4 show the areas for which time series of the areal sea ice area (SIA) shown in Fig. 2b were calculated. **b** The Canada Basin. The zonal band in the blue box, 74.4°–77°N, 130°–160°W, shows the area for which time series of  $\nabla \times \bar{u}_W$  and  $\nabla \times \bar{u}_I$ , shown in Fig. 4b and c, were calculated. The black hashed box, 74.4°–77°N, 150°–160°W, is the area used to calculate time series of the spatial average of ocean dynamic height (ODHc) shown in Fig. 4d

cm for the past 10 years (shown later), which was not large enough to be detected by the accuracy of the altimeter data (~15 cm) (Kwok and Morison 2011). Therefore, we adopted a different approach, based on the Sverdrup relation to evaluate variations, in which oceanic velocities are calculated by vorticity inputs at the sea surface.

In the case of the upper ocean circulation driven by only Ekman pumping without any wave propagation and lateral vorticity inputs, the upper ocean circulation simultaneously responds to surface forcing (Proshutinsky et al. 2002). The observational evidence, however, showed that the spatial pattern of the OBG did not correspond to that of the overlying sea ice gyre (we will refer to this later). As such, the

spatial inconsistency suggests that there was a time lag in the response of the OBG relative to surface forcing. Therefore, the time scale of this delayed oceanic response significantly influences oceanic heat transportation into the basin and the resulting sea ice variations. As a first step toward understanding oceanic influences on sea ice variations, we examined the relative contributions of past surface forcing to the current state of the OBG. The quantitative result enables us to forecast volume transports of the OBG within a time scale that is shorter than the delayed oceanic response.

This paper is organized as follows. Section 2 describes data collection methods used in this study. In Sect. 3, we review spatial patterns of sea ice reduction, and introduce the importance of oceanic roles on sea ice reduction in the Pacific sector of the Arctic Ocean governed by the OBG. In Sect. 4, the delayed response of the OBG to surface forcing is examined from time series of observed hydrographic, wind, and sea ice motion data. The delayed oceanic response is recognized as a key to understanding actual variations of the summer sea ice cover in the OBG region. In Sect. 5, we develop quantitative examinations of the delayed time scale of the OBG using a multiple regression analysis, and provide a simple model to forecast the state of the OBG. In Sect. 6, we give a summary and a discussion of this study.

## 2 Data description

We use hydrographic data collected under the Joint Western Arctic Climate Studies (JWACS) with CCGS LSSL 2002–2008 (<http://www.who.edu/beaufortgyre>) and R/V Mirai 2002, 2004, and 2008 (<http://www.godac.jamstec.go.jp/darwin/cruise/mirai>), and under the Korea-Polar Ocean in rapid transition (K-PORT) expedition with the Korean icebreaker ARAON 2011 and 2012 (PI: SH Kang, e-mail: shkang@kopri.re.kr). We also use data from XCTD data stations, collected during CCGS LSSL 2009–2012, partly supported by Japan Aerospace Exploration Agency (JAXA) research projects [the International Arctic Research Center (IARC)-JAXA Information System, and the Global Change Observation Mission-Water (GCOM-W)] (PI: K. Shimada, e-mail: koji@kaiyodai.ac.jp).

We analyze sea ice concentration data derived from the National Aeronautics and Space Administration (NASA) team algorithm (Cavalieri et al. 1984), provided by the National Snow and Ice Data Center (NSIDC). We also use sea ice motion data calculated by the maximum cross correlation method, the so-called particle image velocimetry (PIV) method (e.g., Adrian 1991), for brightness temperature images obtained from the Advanced Microwave Scanning Radiometer for Earth observing system (AMSR-E) (Kamoshida and Shimada 2010). In the calculation of

Kamoshida and Shimada (2010), 89 GHz channel data gridded onto a polar-stereo projection (2.08 × 2.08 km) is mainly used. In their calculation, the first three correlation peaks are candidates for the calculation of sea ice velocity vectors. If the direction of the re-analysis 10 m wind is out of the range of ±60° relative to the estimated sea ice vector, the estimated value is judged as an unrealistic vector. They use 10 m wind data provided by the National Center for Environmental Prediction/National Center for Atmospheric Research (NCEP/NCAR) reanalysis (obtained at <http://www.esrl.noaa.gov/psd/>). The accuracy of their daily sea ice velocities was evaluated by comparison with other sea ice motion data measured by the bottom-tracking mode of upward-looking acoustic Doppler current profilers (ADCPs), mounted on subsurface moorings that were located in the Chukchi Borderland area. The root mean square of the difference between the satellite-derived velocities and the actual measured ones by ADCPs was 2.5 cm s<sup>-1</sup> during November 2002 to April 2003. Here, we analyze sea ice velocities averaged from November to June. The accuracy of the averaged velocity is much better than that of the daily one, and is accurate enough to estimate the temporal variations of ODH in the OBG region. For the period in which AMSR-E was not operated, sea ice motions are calculated using brightness temperature images obtained from the following sensors: Scanning Multichannel Microwave Radiometer (SMMR) and Special sensor Microwave/Imager (SSM/I).

### 3 Spatial patterns of sea ice retreat

Figure 2a shows time series of the sea ice area (SIA) in September in the area north of 68°N (hereafter referred to as the entire Arctic Ocean). SIA did not show a constant reduction trend, but accompanied rapid reduction events in 1989–1990, 1998, 2007, and 2012. First, we investigate whether these events occurred in the entire Arctic Ocean or were dominated by specific regions. Figure 2b shows time series of SIA in the four distinct areas (areas 1–4 depicted in Fig. 1a). The rapid reduction in 1989–1990 was led by the reduction in the eastern hemisphere in the Arctic Ocean (areas 2 and 3), where the sea ice motion is characterized by the transpolar sea ice drift (blue and black curves in Fig. 2b). The reduction in this region is interpreted as discharges of sea ice through the Fram Strait, which correlate with variations of climatic indices such as the Arctic Oscillation (Thompson and Wallace 1998) or the Dipole Anomaly that is defined as a second empirical orthogonal function (EOF) mode of sea level pressure in the area north of 70°N (Watanabe et al. 2006; Wu et al. 2006). In this period, in contrast, no significant change was observed in the western hemisphere (areas 1 and 4) (red and grey curves in Fig. 2b). The second rapid reduction in 1998 was led by a

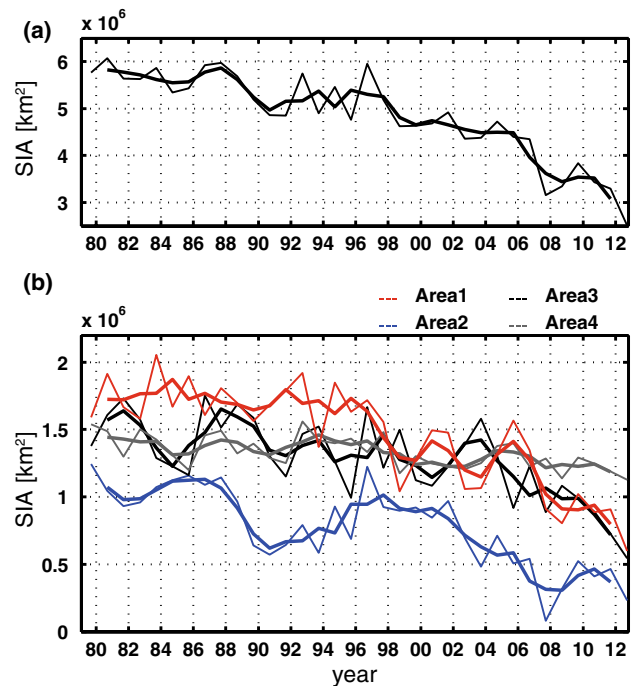


**Fig. 2** Time series of SIA (km<sup>2</sup>) in September, **a** in the entire Arctic Ocean, the area north of 68°N, **b** in the individual four areas depicted in Fig. 1a; area 1 (120°–180°W, red curve), area 2 (140°–180°E, blue curve), area 3 (0°–140°E, black curve), and area 4 (0°–120°W, grey curve). Thick and thin curves denote 3-year running mean values and annual values, respectively

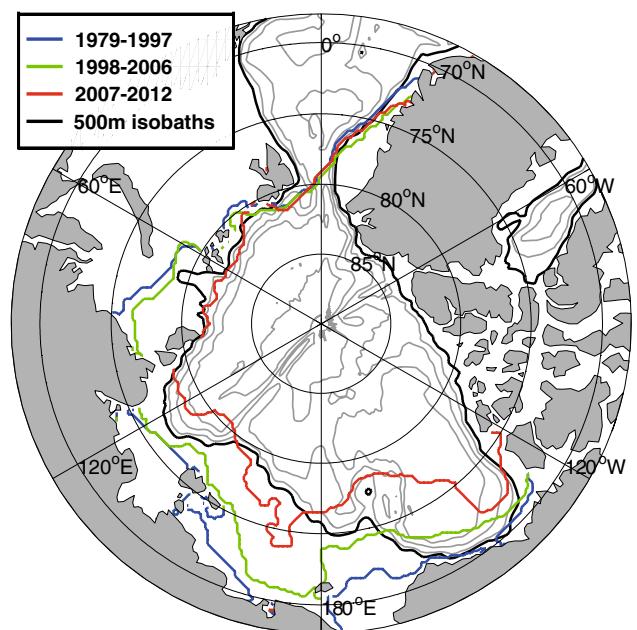


**Fig. 3** Spatial patterns of the ice edge (15 % sea ice concentration) in September, averaged for the following three periods; 1979–1997 (blue curve), 1998–2006 (green curve), 2007–2012 (red curve). Grey contours indicate seafloor topographies deeper than 1000 m, contour interval 1000 m. Black contours denote 500 m isobaths

regional reduction in the Canada Basin (area 1) (red curve in Fig. 2b), without significant changes in other areas (blue, black, and grey curves in Fig. 2b). These regional contrasts suggest that the mechanism of sea ice reduction differs from region to region.

After 1998, the SIA reduction trends in areas 1, 2, and 3 (red, blue, and black curves in Fig. 2b), and also in the entire Arctic Ocean (Fig. 2a), were much larger than those before 1998. In 2012, SIA in the entire Arctic Ocean hit a new minimum record.

Figure 3 shows spatial distributions of the ice edge (15 % sea ice concentration) in September during 1979–1997, 1998–2006, and 2007–2012. Black contours are 500 m isobaths on the continental shelf slopes. During 1979–1997, before the rapid SIA reduction in 1998, open water areas were found only in the shallow shelf regions (blue curve in Fig. 3). During 1998–2006, before the anomalous sea ice reduction in 2007, an embayment-shaped sea ice retreat into the basin was observed in the western Canada Basin (green curve in Fig. 3). In other areas, the ice edges were still located in the shelf regions or on the shelf slopes. During 2007–2012, in the East Siberian and Kara Seas, the ice edges moved offshore but did not enter into the basin deeper than 500 m (red curve in Fig. 3). In the Canada Basin, however, the open water area was enlarged northward along the Northwind Ridge and the Chukchi Plateau, where the major pathway of PSW was identified (Shimada et al. 2001; Steele et al. 2004). This retreat pattern suggests that the oceanic heat carried by the OBG is a key element to understanding the regional sea ice change in the Canada Basin.

#### 4 Oceanic influences on sea ice reduction in the Canada Basin

Shimada et al. (2006) explained that the strengthening of the OBG in the late 1990s was initiated by the strengthening of basin-scale sea ice motion due to less friction of the sea ice cover against the Alaskan Beaufort coast, and then more oceanic heat, leading to the substantial sea ice reduction, was delivered into the deep Canada Basin. Here, we attempt to identify which parameters have controlled the observed temporal variations of the summer SIA in recent years.

##### 4.1 Changes in curls of wind and sea ice velocities

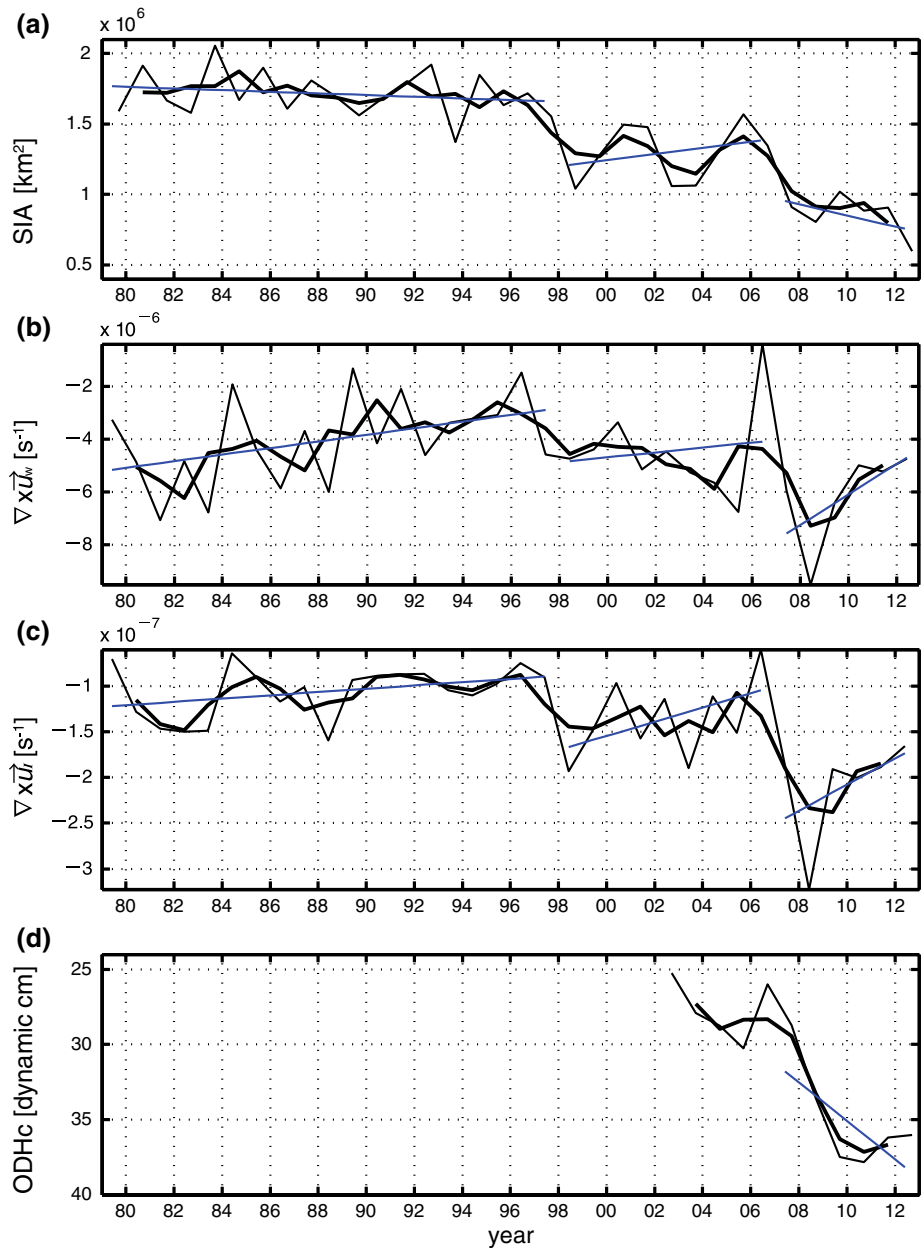
In this section, temporal variations of the surface forcing that drives the underlying OBG are examined. First of all, we briefly mention features of spatial distributions of the OBG, in order to introduce how we can evaluate the volume transport by surface forcing data. In the

climatological mean field, the OBG showed a zonally asymmetric pattern, and its center was located in the region just east of the Northwind Ridge (see Fig. 3 of Shimada et al. 2001). This suggests that the wave dynamics in the presence of the finite amplitude seafloor topography is essential to understanding the zonally asymmetric spatial pattern of the OBG. Sumata and Shimada (2007) explained that the modal exchange from the traveling barotropic Rossby wave to the stagnated baroclinic mode occurred around the wall, due to small planetary  $\beta$  effects, the Northwind Ridge and the Chukchi Plateau, facing to east in the Canada Basin. The non-propagating baroclinic mode formed northward currents within the narrow zonal band over the Northwind Ridge and the Chukchi Plateau. Then, the horizontal shape of the OBG resulted in the zonally asymmetric pattern, just like the mid-latitude subtropical gyre. Such spatial patterns were also found in our hydrographic data analysis, while spatial patterns of the overlying sea ice gyre showed large inter-annual variations (we will argue this in detail in Sect. 4.2). Thus, based on the Sverdrup relation, the vertically averaged volume transport of the OBG would be given by just the surface torque.

Figure 4b and c show time series of curls of 10 m winds and sea ice velocities,  $\nabla \times \vec{u}_W$  and  $\nabla \times \vec{u}_I$ , averaged for the ice-covered period from November to June in the zonal band, in the blue box depicted in Fig. 1b, respectively. Since the climatological Ekman vertical velocity was very weak during July to September (Yang 2006), the curls during that period were ignored in the present study. The curls in October were also neglected, because the sea ice condition in the Canada Basin in that month makes it difficult to quantify relative contributions of winds and sea ice motions to the formation of the OBG. We assumed that drag coefficients at atmosphere–ice and ice–ocean interfaces were constant during November to June in our analysis period. Hereafter, we define the averaged wind curl from November 2011 to June 2012 as  $\nabla \times \vec{u}_W$  in 2012.

During 1979–1996,  $\nabla \times \vec{u}_W$  increased (Fig. 4b), while there were no significant changes in both  $\nabla \times \vec{u}_I$  (Fig. 4c) and SIA in the Canada Basin (Fig. 4a). This suggests that vorticities of surface winds did not penetrate into sea ice under the heavy ice condition during this period (Shimada et al. 2006). From 1997 to 2004,  $\nabla \times \vec{u}_I$  decreased (Fig. 4c) coherently with a decrease in  $\nabla \times \vec{u}_W$  (Fig. 4b). This suggests that the ratio of the sea ice velocities, which are tangential to wind vectors, to the wind velocities, which is a proxy of the kinematic coupling between atmosphere and sea ice (Kimura and Wakatsuchi 2000), was getting larger than that before 1997. When the anomalous summer sea ice reduction was observed in 2007–2008 (Fig. 4a), both  $\nabla \times \vec{u}_W$  and  $\nabla \times \vec{u}_I$  decreased substantially, i.e., clockwise rotations were strengthened (Fig. 4b, c).

**Fig. 4** Time series of **a** SIA ( $\text{km}^2$ ) in September in the Canada Basin (area 1 depicted in Fig. 1a); **b** spatial averages of  $\nabla \times \bar{u}_W$  ( $\text{s}^{-1}$ ) in the ice-covered period (November–June) in the zonal band in the blue box depicted in Fig. 1b; **c** the same as **b**, but for  $\nabla \times \bar{u}_I$  ( $\text{s}^{-1}$ ); **d** spatial averages of ODH (dynamic cm) at 100 dbar relative to 800 dbar in summer (July–September) in the black hashed box depicted in Fig. 1b, ODHc. The z-axis in **d** is inverted. In **a–d**, *thick* and *thin* curves denote 3-year running mean values and annual values, respectively. *Blue straight lines* denote trends of each observe variable in 1979–1997, 1998–2006, and 2006–2012, calculated by a least-squares technique



After 2009,  $\nabla \times \bar{u}_W$  rebounded to the value observed around 2004 or in the mid 1980s (Fig. 4b).  $\nabla \times \bar{u}_I$  also rebounded after 2009, but the rebound did not reach the levels of the 3-year running mean values before 2007 (Fig. 4c). Even though the curls rebounded, SIA in the Canada Basin continued to decrease after 2009 (Fig. 4a). This implies that the observed variations of SIA in the Canada Basin cannot be explained by just the surface forcing, and some oceanic delayed processes, i.e., “ocean inertia” effects, may be necessary to interpret the observed SIA variations after 2007–2008. Before we examine the delayed temporal response of the OBG to the surface forcing, we review recent variations of the OBG, as well as the heat content in the subsurface layer

(25–150 m) in the western Canada Basin where the warm PSW is delivered.

#### 4.2 Changes in the OBG and ocean heat content

Figure 5 shows ODH distributions at 50, 100, and 150 dbar relative to 800 dbar in the summers (July–September) of 2004, 2008, 2011, and 2012 (color). For these four summers, hydrographic observations covering the OBG region are available. Sea ice motions in preceding ice-covered periods (November–June) are also overlaid as vectors. In the summers of 2004, 2011, and 2012, ODH showed patterns that were almost the same at the three levels (Fig. 5a, c, d). In the summer of 2008, however, the pattern of ODH

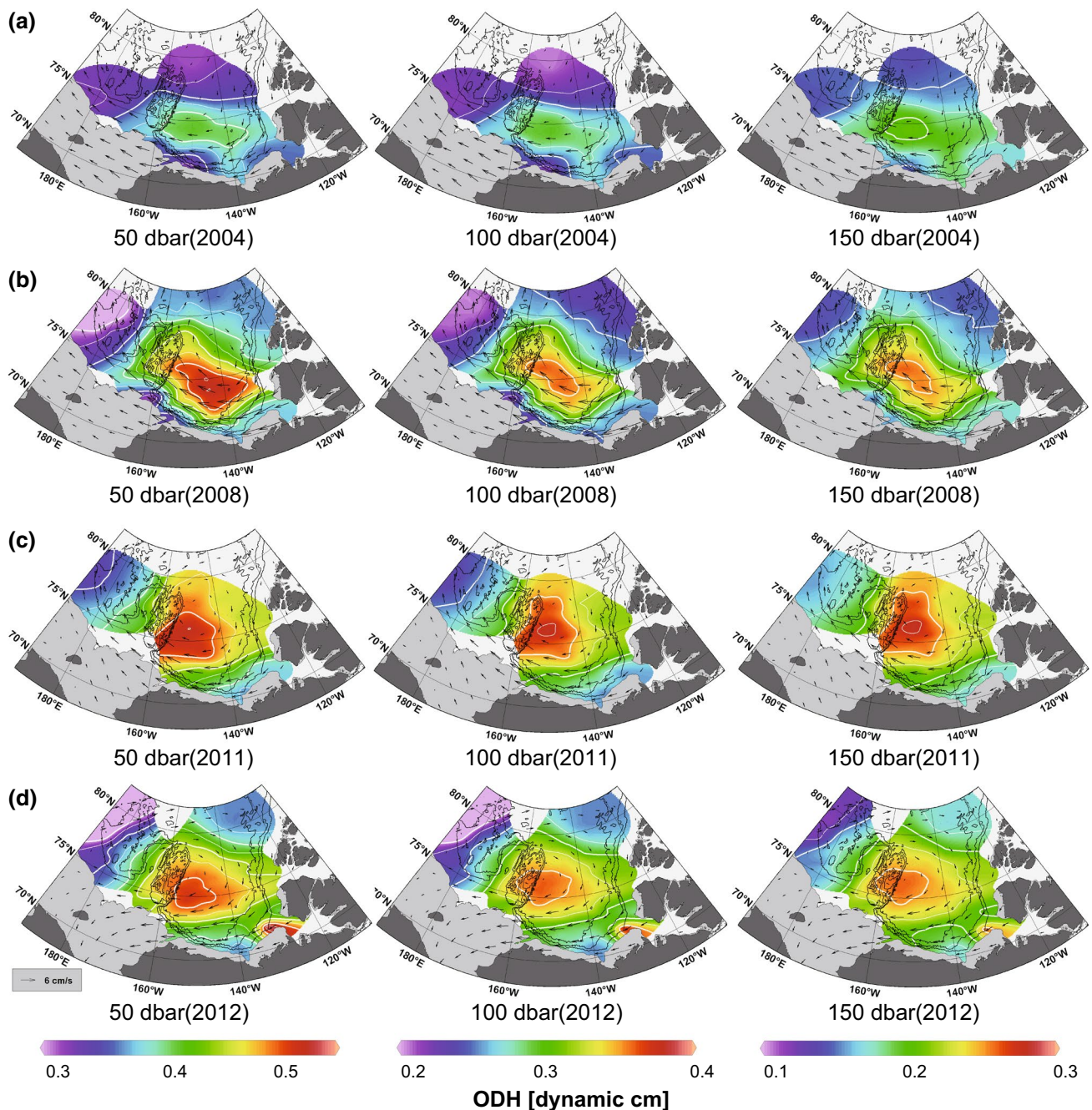


**Fig. 5** Spatial distributions of ODH (color, dynamic cm) at 50, 100, and 150 dbar relative to 800 dbar in summer (July–September) of **a** 2004, **b** 2008, **c** 2011, and **d** 2012, and sea ice motions (vector,  $\text{cm s}^{-1}$ ) in preceding ice-covered period (November–June)

at 50 dbar (left panel of Fig. 5b) slightly differed from the patterns at the deeper levels of 100 and 150 dbar (center and right panels of Fig. 5b). The center of the OBG at 50 dbar in 2008 was not localized just east of the Northwind Ridge, but showed a zonally broad pattern extending southeastward, toward the Canadian Beaufort Sea (left panel of Fig. 5b). The freshwater inputs arising from the melting of multi-year ice anomalously increased in the

summers of 2007 and 2008 in the Canadian Beaufort Sea (Yamamoto-Kawai et al. 2009; Kwok and Cunningham 2010). These freshwater inputs would cause the broadening of the pattern of ODH at 50 dbar observed in the summer of 2008. In 2008, at deeper levels, the center of the OBG was observed at almost the same location, just east of the Northwind Ridge (center and right panels of Fig. 5b), as in the other 3 years (center and right panels of Fig. 5a, c, d).

The observational evidence suggests that the influence of the melt water inputs on the circulation pattern was small at levels deeper than 100 dbar. Therefore, the changes and distributions of ODH at these deeper levels would mainly be established by the dynamical response to the kinematic surface forcing.

At 100 and 150 dbar, northward currents in the zonally narrow area of the Northwind Ridge and the Chukchi Plateau were observed in all 4 years (color in center and right panels of Fig. 5a–d), while overlying sea ice motions were westward in these regions, i.e., sea ice velocity vectors were perpendicular to the direction of the oceanic geostrophic flows (vector in Fig. 5). Such discrepancies in the spatial patterns of the oceanic and sea ice gyres support the notion of a significant role of finite amplitude seafloor topographic features, the Northwind Ridge and the Chukchi Plateau, in the formation of the OBG, as pointed out by Sumata and Shimada (2007). In such cases, the difference in ODH values between the center and rim of the gyre is proportional to the volume transport, based on the Sverdrup relation. Turning to the eastern rim of the OBG, near the Banks Island in the Canadian Archipelago, the ODH values did not change significantly year to year at any of the three levels (Fig. 5). Hence, we can assume the ODH value near the stable center of the OBG as a proxy of the volume transport. Here, we define the spatial average of ODH in the black hashed box depicted in Fig. 1b as a proxy of the northward volume transport. This spatial average of ODH is hereafter referred to as ODHc. The subscript c denotes the “center” of the OBG.

Figure 4d shows temporal variations of ODHc at 100 dbar, which correspond to the lower level of the PSW layer, relative to 800 dbar. The z-axis in the figure was inverted. The annual value of ODHc increased remarkably from 2007 to 2010 (thin curve in Fig. 4d). This shape was similar to those of the 3-year averaged  $\nabla \times \vec{u}_W$  and  $\nabla \times \vec{u}_I$  in 2006–2009 (thick curve in Fig. 4b, c), but ODHc showed time lags of about 2 years relative to the curls. Trends of these observed variables in 2007–2012 indicate that both the loss of SIA (blue line in Fig. 4a) and the volume transport of the OBG (blue line in Fig. 4d) increased, while clockwise rotations of winds and sea ice motions decreased (blue line in Fig. 4b, c). This suggests that the OBG rather than the surface forcing has much more immediate impact on the changes in SIA.

Figure 6 shows time series of potential temperature and salinity near the Northwind Ridge. The thickness of the PSW layer ( $29.5 < S < 32.5$ ; Steele et al. 2004), associated with the oceanic thermal condition affecting the overlying sea ice cover, increased from 2007 to 2010. The thickness was nearly unchanged after 2009, even when the negative vorticity inputs by surface forcing decreased after 2009 (Fig. 4b, c). This suggests that the delayed response of the

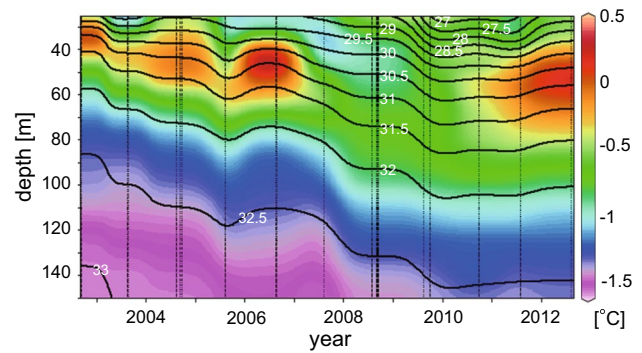


**Fig. 6** Hovmoeller diagram of depth-averaged potential temperature (color, °C) and salinity (black contour), using spatially averaged values in the region near the Northwind Ridge, the black hashed box depicted in Fig. 1b

OBG to surface forcing is a potential candidate for maintaining lateral heat fluxes to the basin. This delayed oceanic response enables us to forecast the upper ocean state from the surface forcing in past years. In the following section, we attempt to construct a simple practical model to estimate the northward volume transport of the OBG without any hydrographic data.

### 5 Temporal response of the OBG to surface forcing

#### 5.1 Multiple regression model to reconstruct temporal variations of ODHc

To reconstruct the temporal variations of the volume transport of the OBG without in situ hydrographic data, relative contributions of curls of winds and sea ice velocities in past years to ODHc is examined. This quantitative examination enables us to estimate the time scale of the delayed response of the OBG to surface forcing. For this purpose, we consider the following multiple regression model, which reconstructs the temporal variations of ODHc using  $\nabla \times \vec{u}_W$  or  $\nabla \times \vec{u}_I$ ,

$$y_r(n) = \sum_{m=0}^N A_m x(n - m) + B, \quad m = 0, 1, \dots, M, \quad (1)$$

where  $y_r$  is the reconstructed ODHc, and  $x$  is the observed  $\nabla \times \vec{u}_W$  or  $\nabla \times \vec{u}_I$ . For example, by using  $\nabla \times \vec{u}_I$  to reconstruct ODHc in the year  $n$ ,  $\nabla \times \vec{u}_I$  in years  $n - 0, n - 1, \dots, n - m$  are substituted into Eq. (1), where  $m$  is the time lag between  $\nabla \times \vec{u}_I$  and ODHc. The maximum time lag  $M$  is chosen arbitrarily. If we choose  $M = 2$ , Eq. (1) is constructed from  $\nabla \times \vec{u}_I$  in years  $n - 0, n - 1$ , and  $n - 2$ . Equation (1) in this case is hereafter referred to as “the model with  $\nabla \times \vec{u}_I$  for  $M = 2$ ”.

In this study, ODHc averaged from July of the year  $n$  to September of the year  $n$  is defined as “ODHc in the year  $n$ ”; e.g., ODHc averaged from July 2006 to September 2006 is defined as “ODHc in 2006”. On the other hand,  $\nabla \times \bar{u}_I$  averaged from November of the year  $n - 1$  to June of the year  $n$ , i.e., averaged for the ice-covered period in the year  $n$ , is defined as “ $\nabla \times \bar{u}_I$  in the year  $n$ ”; e.g.,  $\nabla \times \bar{u}_I$  averaged from November 2005 to June 2006 is defined as “ $\nabla \times \bar{u}_I$  in 2006”. Most of hydrographic data from which ODH was calculated were taken in August in the year  $n$ , while the middle of the analysis period of  $\nabla \times \bar{u}_I$  was the first of March in the year  $n$ . Thus,  $\nabla \times \bar{u}_I$  in the year  $n$  originally preceded ODHc in the year  $n$  by about one-half of a year. In Eq. (1), however, the time lag between  $\nabla \times \bar{u}_I$  in the year  $n$  and ODHc in the year  $n$  is simply regarded as zero, i.e.,  $m = 0$ .

The relative contribution of  $x(n - m)$  to  $y_r(n)$  is statistically measured by the regression coefficient  $A_m$  in Eq. (1).  $B$  is a constant.  $A_m$  and  $B$  are calculated by a least squares technique, so as to

$$\sum_n^N \left\{ \sum_m A_m x(n - m) + B - y(n) \right\}^2$$

is minimized, where  $y$  is the observed ODHc. For the maximum time lag  $M$ , there are  $M + 2$  units of unknowns ( $M + 1$  units of  $A_m$  and  $B$ ). These unknowns are calculated by the following  $M + 2$  units of equations:

$$\sum_n^N \{A_m x(n - m) + B - y(n)\} = 0,$$

$$\sum_n^N x(n - m) \left\{ \sum_m A_m x(n - m) + B - y(n) \right\} = 0,$$

$$m = 0, 1, \dots, M,$$

where the second matrix consists of  $M + 1$  units of equations.

### 5.2 Time scale of delayed response of the OBG to surface forcing

Before turning to the examination of relative contributions of the surface forcing in past years to the volume transport, we first reconstruct the temporal variations of ODHc in 2006–2012 using the model for  $M = 0$ , i.e., the model with just the curl in the previous ice-covered period. As we have mentioned in Sect. 4.2, the response of the OBG showed the time lags relative to surface forcing. The maximum value of the annual ODHc was observed in 2010 (thin curve in Fig. 4d), when both curls rebounded from the maximum negative value observed in 2008 (thin curves in

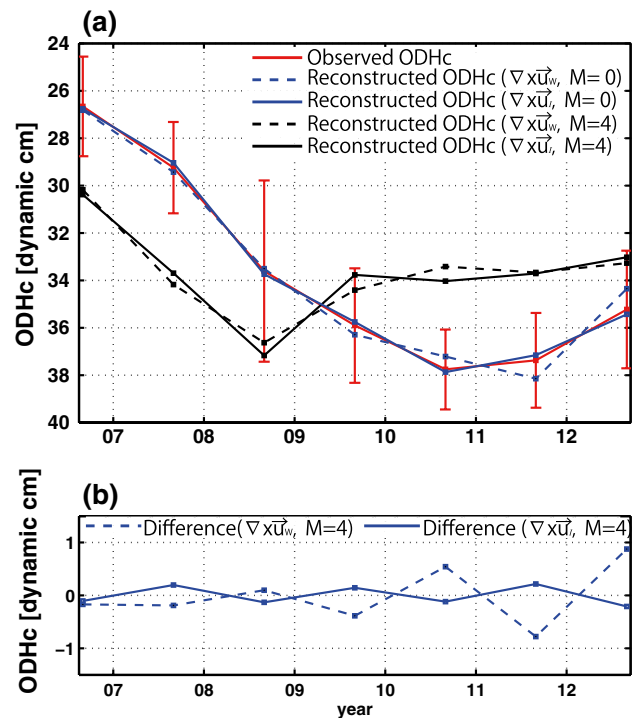


**Fig. 7** Time series of **a** the reconstructed ODHc from the models for  $M = 0$  (black curves) and for  $M = 4$  (blue curves), with the observed ODHc (red curve) (dynamic cm). Bars represent standard deviations of the observed ODH in the black hashed box depicted in Fig. 1b in each summer. **b** Differences between observed and reconstructed ODHc in the case using the models for  $M = 4$ . In **a**, **b**, dashed and solid curves show the reconstructed results from the models with  $\nabla \times \bar{u}_W$  and  $\nabla \times \bar{u}_I$ , respectively

Fig. 4b, c). Thus, we can expect that it is not appropriate to explain the volume transport by just the surface forcing in the previous ice-covered period. The variations of the reconstructed ODHc in 2006–2012 from the models for  $M = 0$  are shown in Fig. 7a (black dashed curve for  $\nabla \times \bar{u}_W$ , black solid curve for  $\nabla \times \bar{u}_I$ ), with that of the observed ODHc (red curve). Indeed, the models for  $M = 0$  did not reconstruct the realistic variations of ODHc. To check the validity of models, we use the square of the correlation coefficient between the observed and reconstructed ODHc (referred to as  $r^2$ ) and the root mean square of the difference between the observed and reconstructed ODHc (referred to as  $D$ ) listed in Table 1.  $r^2$  quantifies the ratio of the observed variations explained by the model. The models for  $M = 0$  explain only about 20 % of the observed variations. In addition,  $D$  are 3.8 and 3.7 dynamic cm for the models with  $\nabla \times \bar{u}_W$  and  $\nabla \times \bar{u}_I$ , which correspond to about 30 % of the amplitude of the observed variations of ODHc in 2006–2012 (11.1 dynamic cm, Table 1). The results suggest that the model should be constructed on the basis of the quantitative examination of the time scale of the delayed oceanic response.

**Table 1**  $r^2$  and  $D$  for models with  $\nabla \times \vec{u}_W$  or with  $\nabla \times \vec{u}_I$

Explanatory variable	$\nabla \times \vec{u}_W$		$\nabla \times \vec{u}_I$	
	$M = 0$	$M = 4$	$M = 0$	$M = 4^a$
Maximum time lag				
$r^2$	0.207	0.982	0.221	0.998
$D$ (dynamic cm)	3.8	0.6	3.7	0.2
The amplitude of the observed variations of ODHc in 2006–2012 (dynamic cm)				11.1

The square of the correlation coefficient between the observed and reconstructed ODHc,  $r^2$  is used to measure the ratio of the observed variations explained by the model.  $D$  is the root mean square of the difference between the observed and reconstructed ODHc

<sup>a</sup>  $M$  is the maximum time lag between the curl and ODHc in Eq. (1)

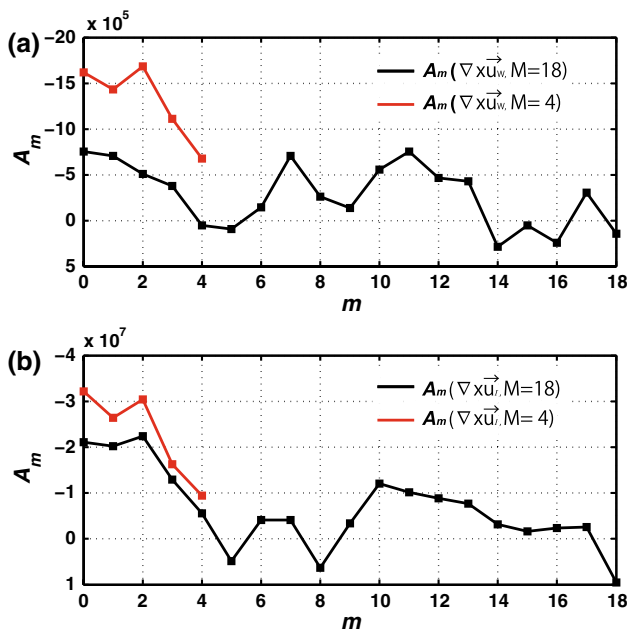


**Fig. 8** Regression coefficients  $A_m$  of the models with **a**  $\nabla \times \vec{u}_W$ , **b**  $\nabla \times \vec{u}_I$ . The  $x$ -axis value  $m$  indicates the time lag between the curl and ODHc in Eq. (1). Black and red curves denote  $A_m$  of the models for  $M = 18$  and  $M = 4$ , respectively

Next, using regression coefficients  $A_m$ , we attempt to examine relative contributions of the surface forcing in past years to the volume transport.  $A_m$  in models with  $\nabla \times \vec{u}_W$  and  $\nabla \times \vec{u}_I$  for  $M = 18$  are shown in Fig. 8a and b, respectively (black curves). The amplitudes of  $A_m$  in both models are large for  $m = 0, 1, 2$ , and decrease as  $m$  increases by  $m = 4$ . Since the amplitudes of  $A_m$  drop to nearly zero at  $m = 4$ , it seems reasonable to construct the models from the curls at time lags  $m = 0, 1, 2, 3, 4$ . For  $m > 4$ , however, the amplitudes of  $A_m$  show a wavy-like oscillation. For example,  $A_m$  in the model with  $\nabla \times \vec{u}_I$  shows another peak at  $m = 10$  (black curve in Fig. 8b). Time series of  $\nabla \times \vec{u}_I$

show rapid decreases in 1988, 1998, and 2008 (thin curve in Fig. 4c), suggesting that there was the step-like regime shift in the large-scale sea ice motion, with intervals of 10 years. Since  $A_m$  were calculated from such the temporal variations of  $\nabla \times \vec{u}_I$  with intervals of 10 years, the partial peak of the amplitude of  $A_m$  would appear at  $m = 10$ . Therefore, we herein assume that the wavy-like variations of  $A_m$  for  $m > 4$  appeared by artificial statistical influences. Consequently, we adopt the models for  $M = 4$  to reconstruct the variations of ODHc.

The reconstructed results from the models for  $M = 4$  are shown in Fig. 7a (blue dashed curve for  $\nabla \times \vec{u}_W$ , blue solid curve for  $\nabla \times \vec{u}_I$ ). The reconstructed variations showed good agreement with the observed ones depicted by the red curve. The correlation coefficients between the observed and reconstructed ODHc in 2006–2012 are 0.991 for  $\nabla \times \vec{u}_W$  and 0.999 for  $\nabla \times \vec{u}_I$  (data length  $N = 7$ , the degree of freedom =  $N - 2$ ), respectively. Thus, the reconstructed results are statistically significant at a confidence level of more than 99 %. The models with  $\nabla \times \vec{u}_W$  and  $\nabla \times \vec{u}_I$  for  $M = 4$  explain 98.2 and 99.8 % of the observed variations in 2006–2012, respectively (Table 1). Moreover,  $D$  are 0.6 and 0.2 dynamic cm, i.e., about 5 and 2 % of the amplitude of the observed variations in 2006–2012, respectively. These agreements suggest that it would be adequate to adopt the models constructed from the curls at time lags  $m = 0, 1, 2, 3$ , and 4.  $A_m$  in the models for  $M = 4$  are shown in Fig. 8a for  $\nabla \times \vec{u}_W$  and Fig. 8b for  $\nabla \times \vec{u}_I$  (red curves). The amplitudes of  $A_m$  in both models are relatively large for  $m = 0, 1$ , and 2, suggesting that the surface forcing in the past three ice-covered periods mainly contributed to the volume transport of the OBG. Therefore, the time scale of the delayed response of the OBG to the surface forcing is estimated to be about 3 years.

Finally, we focus on the differences between the observed and reconstructed ODHc in the case using the models for  $M = 4$  (dashed curve for  $\nabla \times \vec{u}_W$ , solid curve for  $\nabla \times \vec{u}_I$  in Fig. 7b). There is the temporal increase in the differences in the case using  $\nabla \times \vec{u}_W$ , while such a tendency is not seen in the case using  $\nabla \times \vec{u}_I$ . This would be due to changes in the strength in the kinematic coupling between winds and sea ice motions. Therefore, the more direct forcing data,  $\nabla \times \vec{u}_I$ , should be adopted for more precise evaluations of the upper ocean circulation.

### 6 Summary and discussion

To estimate the time scale of the delayed response of ice-covered upper ocean circulation to surface forcing, we have examined how the temporal variations of volume transport of the OBG were reconstructed by surface forcing data in past years. From the multiple regression analysis between

**Table 2** Regression coefficients  $A_m$  in the multiple regression model, Eq. (1), constructed from  $\nabla \times \vec{u}_I$  at time lags  $m = 0, 1, 2, 3, 4$ ; i.e., the maximum time lag  $M = 4$

Regression coefficients ( $\times 10^8$ )	$A_0$	$A_1$	$A_2$	$A_3$	$A_4$
	-0.32	-0.26	-0.30	-0.16	-0.09

$A_m$  represents a relative contribution of  $x(n - m)$  to  $y_r(n)$  in Eq. (1)

ODHc as a proxy of the volume transport and the curl of winds or sea ice velocities, the time scale of the delayed oceanic response was estimated to be about 3 years. Taking into account such the response time scale, the multiple regression models employed here were useful to predict ODHc without in situ oceanographic data. There was a temporal increase in errors in the reconstructed results from wind data, while the increase was not found in the case using sea ice motion data. This suggests that the direct forcing data, sea ice motions, should be adopted for the prediction of ice-covered upper ocean circulation.

The results from the multiple regression analysis, presented in Sect. 5.2, indicate that sea ice motions in the past three ice-covered periods mainly contributed to the formation of the OBG. On the basis of this finding, we argue the influence of delayed oceanic responses on sea ice reduction in recent years, using time series of 3-year running mean values of the sea ice area (SIA) in the Canada Basin,  $\nabla \times \vec{u}_I$ , and ODHc (thick curves in Fig. 4a, c, d). Comparing the variations of  $\nabla \times \vec{u}_I$  and ODHc (Fig. 4c, d), the maximum negative value of  $\nabla \times \vec{u}_I$  appeared in 2008, while the maximum ODHc did not appear in 2008, but in 2010. To interpret this time lag, we briefly turn to the regression coefficients of the multiple regression model constructed from  $\nabla \times \vec{u}_I$  at time lags  $m = 0, 1, 2, 3, 4$ ; i.e., the maximum time lag  $M = 4$  (Table 2). The amplitude of the coefficient indicates that the relative contribution of  $\nabla \times \vec{u}_I$  at the time lag  $m = 2$  ( $A_2$ ) is large and comparable with that at the time lag  $m = 0$  ( $A_0$ ). This suggests that the sea ice motion from about 2 years ago contributed highly to the current volume transport. This result agrees with the observed time lag of about 2 years between the variations of  $\nabla \times \vec{u}_I$  and ODHc (Fig. 4c, d).

The delayed response of the OBG to surface forcing relates to the PSW transport into the basin. In the Northwind Ridge area, the thickness of the PSW layer ( $29.5 < S < 32.5$ ; Fig. 6) coherently changed with ODHc (Fig. 4d), suggesting the substantial PSW transport to this region. The PSW temperature (color in Fig. 6), however, did not show a coherent change with ODHc (Fig. 4d). During 2007–2008, there was the cooling in the PSW layer (color in Fig. 6), suggesting an event-like upward heat release. Apart from these years, we focus herein on the variations after 2009. During 2009–2012, the maximum ODHc

was observed in 2010 (Fig. 4d), and the warmest PSW temperature was observed in 2012 (color in Fig. 6). Since PSW is entrained around the Barrow Canyon into the OBG and is carried onto the Northwind Ridge area, it is expected that the advective time of PSW was associated with the time lag between ODHc and the PSW temperature in the Northwind Ridge area. For example, the mean advective velocity from the Barrow Canyon to the Northwind Ridge area was estimated to be about  $1.7 \text{ cm s}^{-1}$ , using the observed ODH distribution at 100 dbar in 2011 (center panel of Fig. 5c). Thus, the advective time resulted in about 2 years. This advective time would explain the delayed variations of the PSW temperature in the Northwind Ridge area (color in Fig. 6) relative to that of ODHc (Fig. 4d). The minimum of the SIA time series was observed in 2012 (Fig. 4a), when the underlying PSW was warmest (color in Fig. 6). The above coupled variations between sea ice and ocean with inertia would be useful for developing a short-term forecast model for sea ice distributions. The detailed mechanism that controls the delayed response of the ocean, which would be associated with spin-up and spin-down processes of the ice-covered upper ocean circulation, should be investigated by theoretical and numerical approaches in future works.

**Acknowledgments** This work was supported by JAXA research projects (IARC-JAXA Information System, GCOM-W), and the Green Network of Excellence (GRENE) Program. This research was a part of the project titled “K-PORT (KOPRI, PM13020)”, funded by the Ministry of Oceans and Fisheries, Korea. We greatly appreciate the efforts of Takashi Kamoshida in developing the sea ice motion data set. We wish to express our appreciation to Dr. Kohei Mizobata and Dr. Daisuke Hirano for their efforts in carrying out hydrographic observations. We also thank the crews of the IBR/V Araon, the CCGS Louis S. St Laurent and R/V Mirai, and the science parties on board, for their cooperation.

## References

- Adrian RJ (1991) Particle imaging techniques for experimental fluid mechanics. *Ann Rev Fluid Mech* 23:261–304
- Cavalieri DJ, Gloersen P, Campbell WJ (1984) Determination of sea ice parameters with the NIMBUS 7 SMMR. *J Geophys Res* 89(D4):5355–5369
- Comiso JC (2012) Large decadal decline of the arctic multiyear ice cover. *J Clim* 25:1176–1193. doi:10.1175/JCLI-D-11-00113.1
- Kamoshida T, Shimada K (2010) Long term sea ice motion dataset in the Arctic from SMMR, SSM/I and AMSR-E. In: Proceedings of the second international symposium on the Arctic research, Tokyo, Japan, 2010, p 125
- Kimura N, Wakatsuchi M (2000) Relationship between sea-ice motion and geostrophic wind in the Northern Hemisphere. *Geophys Res Lett* 27:3735–3738. doi:10.1029/2000GL011495
- Kwok R, Cunningham GF (2010) Contribution of melt in the Beaufort Sea to the decline in Arctic multiyear sea ice coverage: 1993–2009. *Geophys Res Lett* 37:L20501. doi:10.1029/2010GL044678

- Kwok R, Morison J (2011) Dynamic topography of the ice-covered Arctic Ocean from ICESat. *Geophys Res Lett* 38:L02501. doi:[10.1029/2010GL046063](https://doi.org/10.1029/2010GL046063)
- Kwok R, Rothrock DA (2009) Decline in Arctic sea ice thickness from submarine and ICESat records: 1958–2008. *Geophys Res Lett* 36:L15501. doi:[10.1029/2009GL039035](https://doi.org/10.1029/2009GL039035)
- Markus T, Stroeve JC, Miller J (2009) Recent changes in Arctic sea ice melt onset, freezeup, and melt season length. *J Geophys Res* 114:C12024. doi:[10.1029/2009JC005436](https://doi.org/10.1029/2009JC005436)
- Maslanik J, Stroeve J, Fowler C, Emery W (2011) Distribution and trends in Arctic sea ice age through spring 2011. *Geophys Res Lett* 38:L13502. doi:[10.1029/2011GL047735](https://doi.org/10.1029/2011GL047735)
- Polyakov IV, Walsh JE, Kwok R (2012) Recent changes of Arctic multiyear sea ice coverage and the likely causes. *Bull Amer Meteor Soc* 93(145):151. doi:[10.1175/BAMS-D-11-00070.1](https://doi.org/10.1175/BAMS-D-11-00070.1)
- Proshutinsky A, Bourke RH, McLaughlin FA (2002) The role of the Beaufort Gyre in Arctic climate variability: seasonal to decadal climate scales. *Geophys Res Lett* 29(23):2100. doi:[10.1029/2002GL015847](https://doi.org/10.1029/2002GL015847)
- Shimada K, Carmack E, Hatakeyama K, Takizawa T (2001) Varieties of shallow temperature maximum waters in the Western Canadian Basin of the Arctic Ocean. *Geophys Res Lett* 28:3441–3444. doi:[10.1029/2001GL013168](https://doi.org/10.1029/2001GL013168)
- Shimada K, Kamoshida T, Itoh M, Nishino S, Carmack E, McLaughlin FA, Zimmermann S, Proshutinsky A (2006) Pacific Ocean inflow: influence on catastrophic reduction of sea ice cover in the Arctic Ocean. *Geophys Res Lett* 33:L08605. doi:[10.1029/2005GL025624](https://doi.org/10.1029/2005GL025624)
- Steele M, Morison J, Ermold W, Rigor I, Ortmeyer M, Shimada K (2004) Circulation of summer Pacific halocline water in the Arctic Ocean. *J Geophys Res* 109:C02027. doi:[10.1029/2003JC002009](https://doi.org/10.1029/2003JC002009)
- Sumata K, Shimada K (2007) Northward transport of Pacific summer water along the Northwind Ridge in the Western Arctic Ocean. *J Oceanogr* 63:363–378
- Thompson DWJ, Wallace JM (1998) The Arctic Oscillation signature in the wintertime geopotential height and temperature fields. *Geophys Res Lett* 25(9):1297–1300. doi:[10.1029/98GL00950](https://doi.org/10.1029/98GL00950)
- Watanabe E, Wang J, Sumi A, Hasumi H (2006) Arctic dipole anomaly and its contribution to sea ice export from the Arctic Ocean in the 20th century. *Geophys Res Lett* 33:L23703. doi:[10.1029/2006GL028112](https://doi.org/10.1029/2006GL028112)
- Wu B, Wang J, Walsh JE (2006) Dipole anomaly in the winter Arctic atmosphere and its association with sea ice motion. *J Clim* 19:210–225. doi:[10.1175/JCLI3619.1](https://doi.org/10.1175/JCLI3619.1)
- Yamamoto-Kawai M, McLaughlin FA, Carmack EC, Nishino S, Shimada K, Kurita N (2009) Surface freshening of the Canada Basin, 2003–2007: River runoff versus sea ice meltwater. *J Geophys Res* 114 C00A05 doi:[10.1029/2008JC005000](https://doi.org/10.1029/2008JC005000)
- Yang J (2006) The seasonal variability of the Arctic Ocean Ekman transport and its role in the mixed layer heat and salt fluxes. *J Clim* 19:5366–5387. doi:[10.1175/JCLI3892.1](https://doi.org/10.1175/JCLI3892.1)